

Laser vibrometry from a moving ground vehicle

Leaf A. Jiang,* Marius A. Albota, Robert W. Haupt,
Justin G. Chen, and Richard M. Marino

MIT Lincoln Laboratory, 244 Wood Street, Lexington, Massachusetts 02420, USA

*Corresponding author: leaf@ll.mit.edu

Received 19 November 2010; revised 4 February 2011; accepted 7 February 2011;
posted 10 February 2011 (Doc. ID 138429); published 18 May 2011

We investigated the fundamental limits to the performance of a laser vibrometer that is mounted on a moving ground vehicle. The noise floor of a moving laser vibrometer consists of speckle noise, shot noise, and platform vibrations. We showed that speckle noise can be reduced by increasing the laser spot size and that the noise floor is dominated by shot noise at high frequencies (typically greater than a few kilohertz for our system). We built a five-channel, vehicle-mounted, 1.55 μm wavelength laser vibrometer to measure its noise floor at 10 m horizontal range while driving on dirt roads. The measured noise floor agreed with our theoretical estimates. We showed that, by subtracting the response of an accelerometer and an optical reference channel, we could reduce the excess noise (in units of micrometers per second per $\text{Hz}^{1/2}$) from vehicle vibrations by a factor of up to 33, to obtain nearly speckle-and-shot-noise-limited performance from 0.3 to 47 kHz. © 2011 Optical Society of America

OCIS codes: 280.3340, 280.3420, 280.3640.

1. Introduction

Vibrations measured on the ground, structures, and objects are routinely used to determine mechanical properties and anomalies inside natural and man-made materials. Conventional vibration measurements typically employ contact sensors such as geophones, accelerometers, strain gauges, and angle rate sensors [1–3]. The emplacement of such contact sensors is time consuming, especially in large numbers where the demand for area coverage and spatial resolution often makes contact sensing impractical and cost prohibitive.

Laser vibrometry is a non-contact-sensing method that has been used to measure vibrations in a diverse range of applications such as nondestructive testing in civil and mechanical engineering [4,5], engine diagnostics [6], seismic mapping [7], *in situ* measurements of satellite vibration [8], and landmine detection [4,9–13]. Laser vibrometry can provide location accuracy that is comparable to its spot size on the target, typically millimeters to centimeters. Moreover, low-power laser vibrometry can be con-

ducted at significant standoff ranges from the target, ranging from a few centimeters to a few hundred meters while maintaining eye safety [14,15]. Perhaps the most attractive aspect of laser vibrometry is that, if mounted on a moving platform, it may have the capability to dramatically raise area coverage rates and spatial resolution to a point that would enable material property mapping and imaging within reasonable time frames and costs. However, to date, the noise levels produced from the moving platform have overwhelmed the vibration signal well beyond the point of reliable detection.

In this paper, we report the development of a vehicle-mounted, multiple-beam laser vibrometer, and investigate the capabilities of the system when driving. Vehicle-mounted laser vibrometers face two challenges that are addressed by our system. (1) The motion of the laser vibrometer head cannot be distinguished from the motion of the target. The solution for this is to remove the motion of the vehicle by attaching accelerometers to the transmit apertures and subtracting the line-of-sight accelerometer measurements from the laser vibrometer measurements. Subtracting the motion of the transmit apertures from the signal does not remove all platform

vibrations since there is also parasitic coupling of the vehicle vibrations to the optical fibers. Therefore, it is beneficial to also use one of the five optical channels as a reference and subtract the common-mode vibrational disturbances of the fibers to further reduce platform noise. (2) As the laser vibrometer moves with the vehicle, it sees bright and dark spots (“speckle”) because of the coherent nature of laser light. The modulation of the received intensity and phase causes glitches in the measured velocity versus time. We refer to this effect as speckle noise. The solution for speckle noise is to use a large laser spot size (7 mm), which reduces the speckle exchange rate, thereby decreasing speckle noise. In addition, the large depth of field of our laser (thanks to the large spot size) removes the need for electronic autofocus optics.

There are five salient features of our system.

1. Large area coverage: the area coverage rate (platform velocity times swath width) increases proportionally to the number of beams. Five channels were demonstrated in our work, but our architecture is scalable to over 20 channels.

2. Real-time Doppler tracking: the main component that differentiates static laser vibrometers from mobile laser vibrometers is the hardware for tracking Doppler shifts. We report a real-time Doppler tracker implemented in field-programmable gate array (FPGA) hardware. Previous work on mobile laser vibrometers consists mainly of robotic cart-mounted laser vibrometers [13,16–18], where the velocity of the vehicle is carefully controlled using electronic feedback controllers. These earlier mobile laser vibrometers also have no Doppler tracking capability (there is only tracking over the 40 or 50 kHz demodulator bandwidth and not over, say, the 10 MHz Doppler bandwidth) and are therefore limited to slow speeds (e.g., 1.95 cm/s in [13]) and nearly vertical beam paths ($<10^\circ$ angle of inclination), so that the vehicle is on top of the target. It should be noted that [17] reported initial efforts to increase the laser Doppler vibrometer bandwidth from 40 kHz to ± 5 MHz, but the poor sensitivity of the photodiode electronics required the use of retroreflective targets, and all the data were postprocessed instead of processed in real time.

3. Horizontal standoff range: thanks to real-time Doppler tracking, the laser vibrometer can point nearly horizontally (84° angle of inclination) ahead of the vehicle to yield a 10 m range.

4. High sensitivity: the sensitivity of our laser vibrometer is $<40 \mu\text{m/s}$ per $\text{Hz}^{1/2}$ from 30 to 100 Hz and $<10 \mu\text{m/s}$ per $\text{Hz}^{1/2}$ for 100 to 600 Hz at a vehicle velocity of 200 cm/s (see Fig. 11), compared to previously reported results of $\sim 400 \mu\text{m/s}$ per $\text{Hz}^{1/2}$ for 30 to 100 Hz and $\sim 100 \mu\text{m/s}$ per $\text{Hz}^{1/2}$ for 100 to 600 Hz at a platform velocity of 2 cm/s [13]. The 10 \times improvement in sensitivity at low frequencies of our system is mainly attributed to lower speckle noise due to the larger spot size (7 mm in our system versus

$\sim 100 \mu\text{m}$ for some commercial vibrometers) and platform motion compensation using accelerometers and an optical reference channel. Accelerometers (sometimes realized by mounting a mirror on a compliant damper) have been used in previous work on laser vibrometers [19–21] to compensate for platform vibrations, but measurements of the platform vibration rejection ratio as a function of frequency were not reported. In Subsection 3.C, we obtained platform vibration rejection ratios as high as 23 dB using piezoelectric accelerometers.

5. Proven capability in the field: the results presented here were achieved with a human operator in a field-worthy vehicle, resulting in realistic vehicle speed profiles and platform vibrations. It should also be noted that the vehicle was driven on a dirt road and not a smooth paved road.

2. Mobile Laser Vibrometer Design

Our five-channel laser vibrometer was mounted on a high-mobility multipurpose wheeled vehicle. The electronics rack (61 cm \times 91 cm \times 114 cm) is mounted in the back of the truck and consists of the fiber-optic laser system, detectors, real-time processing hardware, data acquisition computer, power inverter, and uninterruptible power supply. The rack was closed-cycle cooled to $\sim 25^\circ\text{C}$ with a 1500 BTU air conditioner. The optical breadboard sits on top of an aluminum plate that is bolted directly to the roof of the vehicle at an elevation of ~ 2 m above ground level. The five transmitters project 7 mm diameter ($1/e^2$) collimated beams to a distance of 10 m in front of the vehicle. The illumination spots, shown in Fig. 1, were arranged in a line in front of the vehicle and with a beam-to-beam spacing of 10 cm. A shortwave infrared (SWIR) camera (Goodrich SU320, 0.8–1.8 μm) and a visible camera were mounted on the optical breadboard to aid with beam alignment and for system diagnostics.

A. Transmitter

The optical system is a bistatic heterodyne-detection laser radar. A diagram of the transmitter is shown in Fig. 2. All fiber pigtails are Corning SMF-28



Fig. 1. Five laser beams incident on a dirt road, located 10 m in front of the vehicle. Image was captured with a SWIR camera.

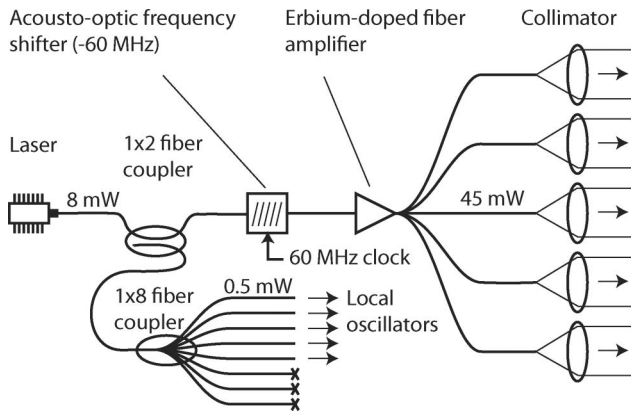


Fig. 2. Multibeam laser vibrometer transmitter. The laser is a Redfern Integrated Optics Orion. The acousto-optic frequency shifter is a Brimrose AMF-60-60 1550-2FP+. The EDFA is a Keyopsys KPS-CUS-OEM-05-28-FA-FA. The collimator mount is a Newport U100-A3K. The collimator is a Thorlabs F810APC-1550.

single-mode fiber. The semiconductor laser (Redfern Integrated Optics Orion) is a narrow-linewidth (<10 kHz), low relative intensity noise (~ 150 dB/Hz at 7 MHz), $1.5\ \mu\text{m}$ wavelength source that maintained coherence in a vibrating environment. The laser output is split by a 1×2 fiber coupler to a transmit arm and a local oscillator arm. The transmit arm contains an acousto-optic frequency shifter that translates the frequency of the light by -60 MHz. The sign was chosen to be negative so that a positive Doppler shift (driving toward the target) decreases the intermediate frequency (IF). As the vehicle velocity goes from 0 to 7.8 m/s, the IF goes from 60 to 50 MHz. The value of 60 MHz was chosen because in addition to being a common frequency for acousto-optic modulators, it is also the frequency at which the relative intensity noise (RIN) of many laser sources (including ours) is shot-noise limited. After the acousto-optic frequency shifter is an erbium-doped fiber amplifier (EDFA) with adjustable gain (via RS-232 port), ~ 5 dB noise figure, >45 dB optical signal-to-noise ratio, and 7% wall-plug efficiency. The output of the EDFA is evenly split into five fibers by a 1×5 single-mode fiber-optic splitter. Each output of the splitter is connected to a collimator, which produces a 7 mm diameter collimated beam. The optical power for each channel is 45 mW, which we intentionally set equal to the American National Standards Institute Z136 maximum permissible exposure power level. The local oscillator arm contains a 1×8 fiber splitter, of which five of the outputs are used as local oscillators for coherent balanced detection. The remaining three terminals of the splitter are terminated into angle-polished connectors (to minimize back reflections into the laser) and were used to monitor the local oscillator power.

B. Receiver

The receiver consists of five channels—each of which contains a balanced detector, a Doppler tracker, and an in-phase quadrature (IQ) demodulator—and data acquisition computer. A diagram of one of the five re-

ceiver channels is shown in Fig. 3. One of the local oscillators from Fig. 2 connects to the local oscillator in Fig. 3.

Balanced detection is typically used to reduce RIN from the local oscillator. To get good common-mode extinction, the 2×2 fiber splitters feeding the balanced detectors were selected to have a split ratio as close to 50/50 as possible, and the lengths of the pigtails from the splitter to the detectors were matched to within 2 cm. Since the RIN of our laser was already shot-noise limited, the only benefit of a balanced detector compared to a single detector is that the balanced detector captures all the return light. Each InGaAs/PIN balanced detector had a responsivity of 1 A/W, a 3 dB bandwidth of 75 MHz, a common-mode rejection ratio of 35 dB, and a gain of 90×10^3 V/A into $50\ \Omega$.

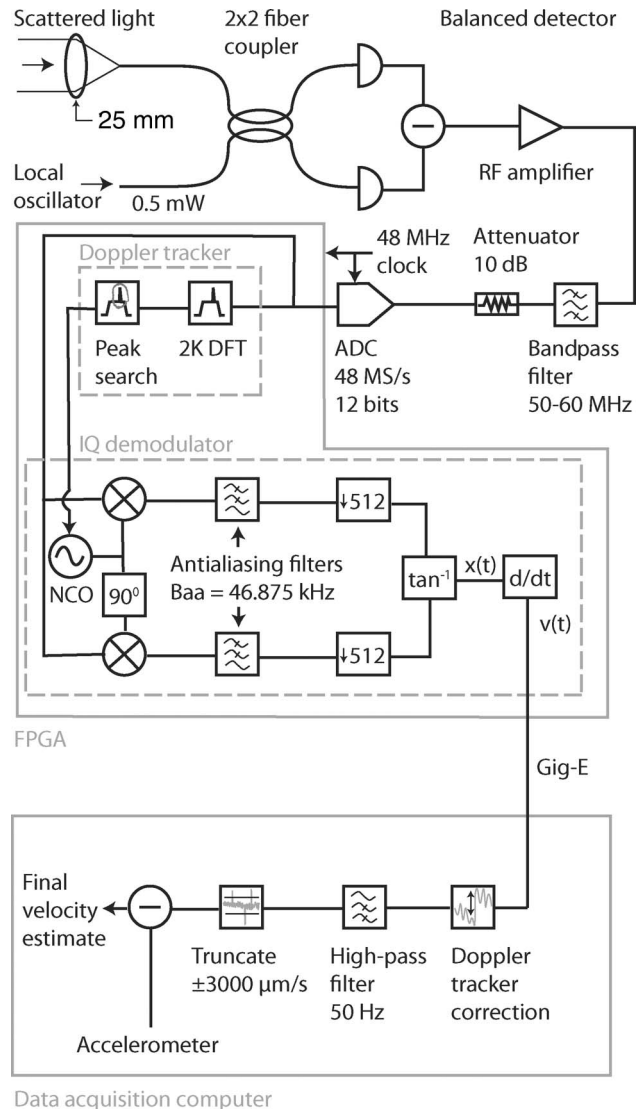


Fig. 3. One of five receiver channels. The balanced detector is a Thorlabs PDB120C-AC. The RF amplifier is a Mini-Circuits ZKL-1R5. The bandpass filter is a K&R Microwave 2435-55-SMA. The ADC is a Linear Technology LTC2209. The FPGA is half of a Xilinx Virtex-5 95SXT. The gray lines show the components that make up the FPGA and data acquisition computer. Gig-E, gigabit Ethernet.

After each balanced detector, an RF amplifier (40 dB gain, 3 dB noise figure), followed by a band-pass filter and an RF attenuator (10 dB), was used to bring the signal level to the middle of the analog-to-digital converter's (ADC's) 1.5 V peak-to-peak input range. The peak voltage of the IF carrier was typically between 10–700 mV, depending on the intensity of the speckle realization. The balanced detector plus RF gain resulted in a net gain of 2.85×10^6 V/W.

The electronic hardware, which includes both the ADC and FPGA, are described in [22,23]. The ADC is a Linear Technology LTC2209 with a specification of 16 bits and 160 MS/s. Because of the electronic noise on the boards, the effective number of bits was 12, but 12 bits was sufficient to account for variations in the light intensity due to speckle and target reflectivity. The ADC was clocked at 48 MS/s to have the sample rate greater than twice the Doppler processing bandwidth ($B_{DP} = 10$ MHz, the RF filter passes signals between 50 and 60 MHz) so that the IF (50–60 MHz) did not alias to 0 Hz (0 Hz is plagued by flicker noise and other noise sources).

The FPGA implements the Doppler tracker and IQ demodulator. Each Virtex-5 95SXT FPGA processes the data from two beams. About 83% of the logic resources are used on the FPGA (90 out of 640 digital signal processor blocks, 106 out of 244 block RAM, and 12,183 out of 14,720 slices). The FPGA continuously processes data with no gaps. Computations are computed over a user-specified interval, T_u , which we typically set to 20 ms (depending on maximum acceleration, see next paragraph), and then the demodulated data are packetized and transmitted over gigabit Ethernet to a rack-mount computer.

Each optical channel has an independent Doppler tracker since the beams fan out in front of the vehicle and experience different Doppler shifts, depending on their angle relative to the vehicle direction. The Doppler tracker is responsible for tuning the numerically controlled oscillator frequency (denoted by NCO in Fig. 3) to match the IF. The NCO mixes the aliased IF carrier (2–12 MHz) into the acceptance bandwidth of the IQ demodulator. The IF varies, depending on the vehicle velocity (50–60 MHz for 7.8–0 m/s, respectively). The Doppler tracker collects 2048 data points at 4.8×10^7 samples/s, computes the power spectrum (shown by the 2048 point discrete Fourier transform (“2K DFT”) block in Fig. 3), and averages the results in block memory. The power spectra are averaged over time T_u , and then the frequency at which a peak is detected in the averaged power spectrum (shown by the “peak search” block in Fig. 3) is used to tune the NCO. Therefore, the NCO is updated at T_u intervals. The spectral bin width of the 2K DFT ($4.8 \times 10^7/2048 = 23.4375$ kHz) was chosen to be less than $2B_{aa} = 93.750$ kHz (where B_{aa} is the bandwidth of the antialiasing filter), i.e., the following constraint must be met: $T_u^{-1} < 2B_{aa}$. The Doppler tracker can handle accelerations up to $|a| \leq \lambda B_{aa}/(2T_u)$. For $B_{aa} = 46.875$ kHz and $T_u =$

20 ms, $|a| \leq 1.8$ m/s². This performance was sufficient for our experiments, but at higher accelerations, either B_{aa} must be increased or T_u must be decreased. When the Doppler tracker cannot keep up with changes in the vehicle velocity, the output velocity versus time has random values of velocity between $\pm \lambda B_{aa}$.

The IQ demodulator extracts the phase of the IF carrier (the output of the arctangent block in Fig. 3), which is proportional to the surface displacement of the target according to $\theta = 2kx = (4\pi/\lambda)x$. The vibration velocity, $v(t)$, is simply estimated by computing the derivative of the displacement (shown by “d/dt” in Fig. 3). The bandwidth of the antialiasing filter, B_{aa} , must be large enough to account for the largest vibrational frequency of interest (a lower bound is given by Carson's rule [24], p. 184) and the maximum acceleration of the Doppler tracker.

Not included in the diagram for the FPGA are Inter-Range Instrumentation Group (IRIG) and 1 pps inputs for time stamping data. Time stamping is important for correlating with external sensors, such as accelerometers on the vehicle or laser head. In addition, there is an ADC DC bias cancellation circuit after the ADC that averages the DC value and subtracts the DC value from the data. The packetized data contain the *I* and *Q* data, the velocity versus time, the IRIG time stamp, the global positioning system location, the NCO frequency, the averaged power spectrum used in the Doppler tracker, and several overflow diagnostic bits for various locations in the processing chain.

The data packets are transmitted from each micro-telecommunications-computing-architecture card (each card handles two optical channels) to the data acquisition computer. The computer stores the data packets to disk and has a real-time display showing the power spectrum, the demodulated power spectrum computed over T_u , the location of the vehicle on a map, and the SWIR video.

The functions shown in the data acquisition computer in Fig. 3 were actually postprocessed (not real time). The Doppler tracker (shown inside the data acquisition computer in Fig. 3) removes discontinuities due to the Doppler tracker. When the NCO changes frequency, it occurs discretely at intervals of T_u and results in instantaneous jumps in $v(t)$ with magnitude proportional to the frequency change. Since the value of the NCO is reported with the data packet, we simply add a velocity offset proportional to the frequency change to the $v(t)$ data at the instant of time that the NCO was tuned. The result is a smooth waveform. After the Doppler tracker is a high-pass filter that removes the DC and low-frequency variations and prepares the waveform for the following truncation operation. In our computations, we arbitrarily truncate the vibration velocity, keeping only values between ± 3000 μ m/s. Random speckle phase variations manifest as spikes in $v(t)$ with very large amplitudes. By truncating the spikes, the resulting white noise in the demodulated spectrum can be

reduced. Other methods for spike reduction in the velocity versus time signals are summarized in [25]. Finally, the accelerometer data (or another optical channel) can be subtracted from $v(t)$. In our system, an accelerometer was mounted to the face of each transmit collimator mount. The accelerometer data can be subtracted “coherently” as shown here, or it can be subtracted “incoherently” by simply subtracting power spectra. All the data presented here use coherent subtraction. The power spectrum of the final velocity estimate is then computed over the minimum dwell time T_{dw} . The minimum dwell time used in this work was 1 sand is equal to the desired spatial resolution divided by the desired vibrational frequency resolution. Because of inherently large platform vibrations at low frequencies, it is advantageous to use a window whose spectral tail decays rapidly, such as the Blackman window (40 dB/decade), rather than the rectangular window (20 dB/decade).

3. Noise Sources

The performance of a mobile laser vibrometer is determined by its noise floor. The noise floor consists of the following components: shot noise that dominates the noise floor at high acoustic frequencies (>5 kHz), speckle noise that mainly contributes noise energy to low frequencies (<1 kHz), and platform vibration noise, which typically manifests at low frequencies (<0.5 kHz). The noise sources of heterodyne laser radar systems have been analyzed previously (see, for example, [26,27]), and we extend this work by deriving simple, analytical expressions for the vibration amplitude spectrum due to shot and speckle noise for the case of high carrier-to-noise ratio (CNR). The results in this section are limited to spectrogram processing of a continuous wave (CW) transmitter and are not directly applicable to pulse-pair or poly-pulse emissions. A comparison of processing techniques can be found in [28]. Furthermore, when the CNR is small, the nonlinear coupling between the additive (shot) and multiplicative (speckle) noise becomes significant, and hence the resulting spectral functional form becomes more complicated [29]. Here we only consider the high-CNR case, since it is easily achieved at ranges of 10 m.

A. Shot Noise

Shot noise arises due to statistical fluctuations in measurements. In this section, we derive a simple expression for the shot-noise floor of a laser vibrometer for the case of high CNR and compare the theoretical expressions to measured data. The detected current for a heterodyne ladar is

$$i(t) = i_{LO} + i_S(t) + 2\sqrt{\eta_h i_{LO} i_S(t)} \cos(\omega_{IF}t + \theta(t)), \quad (1)$$

where i_{LO} is the current from the local oscillator, i_S is the current from the signal, η_h is the heterodyne mixing efficiency (0 to 1), ω_{IF} is the IF, and $\theta(t)$ is the phase shift. The IF frequency ω_{IF} is equal to the acousto-optic modulator frequency offset plus the

Doppler offset due to the forward vehicle motion and is 50–60 MHz for our system. The phase shift $\theta(t)$ is given by

$$\theta(t) = 2kx(t) + \theta_S(t) = \frac{4\pi x(t)}{\lambda} + \theta_S(t), \quad (2)$$

where $x(t)$ is the line-of-sight distance between the ladar and the target, $\theta_S(t)$ is the random phase of the speckle lobe, and λ is the optical wavelength. $x(t)$ changes because of target vibrations, vehicle vibrations, and pointing jitter. For diffuse targets, $\theta_S(t)$ is random and uniformly distributed from $-\pi$ to π for each speckle lobe (e.g., for each illuminated spot). It is a function of time since it is assumed that the beam moves across the target due to either horizontal vehicle motion or pointing jitter.

The Fourier transform of Eq. (1), at frequency ω_{IF} , is equal to $c + n$, where

$$c \equiv |c| \exp(j\theta) = \sqrt{\eta_h i_{LO} i_S} \exp(j\theta) \quad (3)$$

is the carrier and n is the shot noise. The time dependence of θ in Eq. (3) is removed since it is slow compared to ω_{IF} : the bandwidth of $x(t)$ is at most tens of kilohertz and the bandwidth of $\theta_S(t)$ is about a kilohertz or less. n is a two-dimensional Gaussian distribution in the real–imaginary plane [30], and the classic graphical representation of c and n in the complex plane is a phasor, c , plus a random phasor sum, n (often drawn as a line plus circle in the complex plane) [31] (see Fig. 4). The rms value of $|n|$ is $n_{rms} = \sqrt{2q i_{LO} B_{aa}}$, where $B_{aa} = 46.875$ kHz is the single-sided bandwidth of the antialiasing filter.

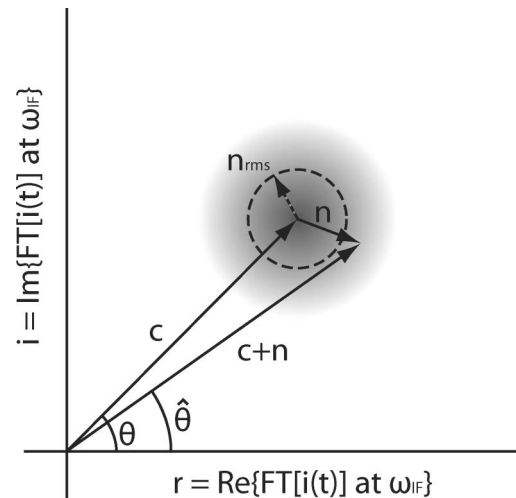


Fig. 4. Phasor diagram for carrier and noise. The carrier, c , is given by Eq. (3). The noise, n , is two-dimensional Gaussian distributed with probability density function $\exp[-(r^2 + i^2)/(2n_{rms}^2)]/(2\pi n_{rms}^2)$. The dashed circle with radius n_{rms} denotes the standard deviation of the two-dimensional Gaussian distribution. The magnitude of the noise, $|n|$, is Rayleigh distributed. The estimate of the carrier’s phase, $\hat{\theta}$, is one-dimensional Gaussian distributed for $|c| \gg |n|$. “FT $[i(t)]$ ” denotes the Fourier transform of the detected current given by Eq. (1).

The CNR is measured from the power spectrum of the detected current and is equal to (peak-background)/background. In other words, it is equal to the ratio of the power at the IF (minus background) to the background rms noise value at the IF:

$$\text{CNR} \equiv \frac{\text{carrier power}}{\text{noise power}} = \frac{E[|c|^2]}{n_{rms}^2} = \frac{\eta_h i_S}{2qB_{aa}} = \frac{\phi_{pe}}{2B_{aa}}, \quad (4)$$

where $E[\cdot]$ is the expectation value computed over all possible speckle realizations (i.e., all possible values of i_S), ϕ_{pe} is the received photoelectrons per second, and q is the electron charge. The CNR is simply the ratio of the received signal photoelectron rate divided by the demodulated bandwidth of the vibrometer. The CNR is typically measured by probing the signal after the attenuator in Fig. 3 with an RF spectrum analyzer (instead of an actual RF spectrum analyzer, we simply captured and displayed the data after the 2K DFT block in Fig. 3) and averaging the measured spectrum over all speckle realizations (with constant vehicle speed so that the carrier occupies only one IF bin). The carrier-plus-noise power, $|c|^2 + |n|^2$, is then directly read from the spectrum analyzer at ω_{IF} —the so-called “peak.” The noise power, $|n|^2$, is estimated by averaging the spectrum analyzer values in the frequency bins next to the IF bin—the so-called “background.” The noise power is integrated over a bandwidth of $2B_{aa}$. As will be shown later, the CNR determines the shot-noise level in the demodulated spectrum.

As shown in Fig. 4, the carrier-plus-noise phasor subtends a new angle $\hat{\theta}$, which approximates the angle of the carrier, θ , when the noise is small. Therefore, in subsequent derivations, we will use $\hat{\theta}$ to approximate θ . The standard deviation of $\hat{\theta}$ is

$$\hat{\theta}_{rms} \sim \frac{n_{rms}}{E[|c|]} = \frac{1}{\sqrt{\text{CNR}}}, \quad (5)$$

where the first approximation assumes a properly designed vibrometer with large CNR ($|c| \gg |n|$), and the last equality comes from Eq. (4). The shot-noise spectrum for $\hat{\theta}$, $S_{\theta}(f)$, is flat (constant) from $-B_{aa}$ to $+B_{aa}$, and is related to the variance of $\hat{\theta}$ by

$$(\hat{\theta}_{rms})^2 = \int_{-B_{aa}}^{+B_{aa}} S_{\theta}(f) df. \quad (6)$$

Solving for $S_{\theta}(f)$ yields

$$S_{\theta}(f) = \frac{(\hat{\theta}_{rms})^2}{2B_{aa}} = \frac{1}{2B_{aa}\text{CNR}} = \frac{1}{\phi_{pe}} \quad (7)$$

for $-B_{aa} \leq f \leq +B_{aa}$, and zero otherwise.

In the absence of speckle, $\theta(t) = 2kx(t)$. Under this condition, $S_{\theta}(f)$ is related to the shot-noise spectrum for the surface displacement x , $S_x(f)$, by

$$S_x(f) = \left(\frac{\lambda}{4\pi}\right)^2 S_{\theta}(f) \quad [\text{m}^2 \text{ per Hertz}]. \quad (8)$$

We are now in the position to write an expression for the noise spectrum of the surface velocity, $S_v(f)$. Since $v = dx/dt$, the Fourier transforms are related by $V(f) = j2\pi f X(f)$, and $S_v(f)$ is related to $S_x(f)$ by

$$S_v(f) = (2\pi f)^2 S_x(f) = \left(\frac{\lambda}{4\pi}\right)^2 (2\pi f)^2 S_{\theta}(f) \quad [(\text{m/s})^2 \text{ per Hertz}]. \quad (9)$$

The literature usually reports a single-sided ($0 \leq f < \infty$) amplitude noise spectrum of the surface velocity, resulting in a factor of 2 difference compared to $S_v(f)$. Furthermore, the amplitude noise spectrum refers to the peak velocity rather than the rms velocity (another factor of 2 difference), so the amplitude (shot) noise spectrum for the surface velocity $A_{v,sh}$ is given by

$$\begin{aligned} A_{v,sh}(f) &= \sqrt{\underbrace{2}_{\text{rms to peak}} \times \underbrace{2}_{\text{double to single sided}} \times S_v(f)} \\ &= 2 \left(\frac{\lambda}{4\pi}\right) (2\pi f) \sqrt{S_{\theta}(f)} = \frac{f\lambda}{\sqrt{\phi_{pe}}}. \end{aligned} \quad (10)$$

Typical units are micrometers per second (peak) per $\text{Hz}^{1/2}$.

Equation (10) shows that the shot-noise amplitude spectrum for the peak surface velocity increases linearly with vibration frequency and is inversely proportional to $\text{CNR}^{1/2}$. This may be surprising to some laser vibrometer users since the noise floor looks flat over small (less than a few kilohertz) frequency spans. The linear nature of the noise floor is apparent when looking over tens of kilohertz [see Fig. 5(a)].

To get an expression for the shot-noise amplitude spectrum for the peak surface displacement, simply divide Eq. (10) by $2\pi f$. Therefore, the surface displacement amplitude spectrum is independent of frequency:

$$A_{x,sh}(f) = \frac{\lambda}{2\pi\sqrt{\phi_{pe}}}, \quad (11)$$

with units of meters (peak) per $\text{Hz}^{1/2}$.

The measured shot-noise amplitude spectra for velocity and displacement are shown in Figs. 5(a) and 5(b), respectively. These data did not include speckle noise since the vehicle was not moving at the time. The integration time was 1s, $\text{CNR} = 37.1 \text{ dB}$, $B_{aa} = 46.875 \text{ kHz}$, and $\phi_{pe} = 4.8 \times 10^8$ photoelectrons per second. Figure 5(c) shows the histogram of Fig. 5(b) from 10 to 46.875 kHz (below 10 kHz, the noise contains vehicle vibrations and other non-shot-noise sources, and hence is not included in forming the histogram). The straight black line in Fig. 5(a) comes from Eq. (10). The solid

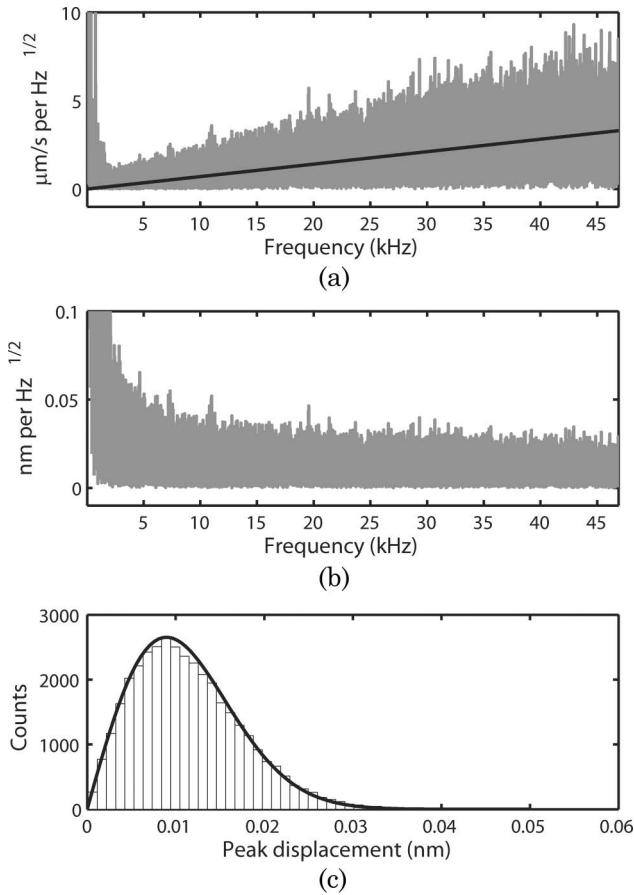


Fig. 5. Measurements from a parked vehicle. (a) Plot of the surface velocity amplitude spectrum, $A_{v,sh}(f)$. (b) Plot of the surface displacement amplitude spectrum, $A_{x,sh}(f)$. (c) Histogram of the displacement amplitude spectrum from 10 to 46.875 kHz.

black curve in Fig. 5(c) shows a Rayleigh probability density function with mean equal to Eq. (11) and provides an excellent fit to the histogram of the measured data. The magnitude of a random variable that has a two-dimensional Gaussian distribution is Rayleigh distributed ([31], p. 49): n is two-dimensional Gaussian distributed, so $|n|$ is Rayleigh distributed with mean $A_{x,sh}$. It can be seen that Eq. (10) is an accurate expression for the shot-noise floor at high CNR.

In this section, the CNR was found to be constant because the vehicle was not moving, but as we will see in Subsection 3.B, the CNR changes as a function of time because bright and dark speckles traverse the receive aperture as the vehicle moves.

B. Speckle Noise

Speckle noise occurs when the laser spot traverses a beam diameter on a rough target due to pointing jitter or horizontal motion of the vehicle. There is no speckle noise when the vehicle is stationary. As the spot moves, the receiver is swept through a number of speckle lobes that have random intensity (negatively exponentially distributed) and phase (uniformly distributed). The phase jumps manifest

as “glitches” in the velocity versus time output of the laser vibrometer. Increasing the spot size reduces the number of phase jumps per unit time and thereby reduces the noise floor (a derivation of the degree of coherence for object translation is given in [32]). The prediction of the vibration amplitude noise floor due to speckle at low frequencies is given by Eq. 4 in [33] and Eq. 10 in [34] (both formulas agree to within a factor of $2^{1/2}$ at high CNR). Dräbenstedt [34] carefully measured the speckle noise floor by moving a rough surface transversely to the laser vibrometer beam. The experiments were carried out at high CNR so that the shot-noise contribution would be much smaller than the speckle noise contribution to the noise floor. He found that the resulting speckle noise spectrum fit well to a piecewise-continuous function: constant below the exchange rate of the speckle pattern (denoted by f_{exc}) and $1/f$ above f_{exc} . In this work, we postulate that the speckle noise follows the square root of a Lorentzian function since the Lorentzian function (1) exhibits Dräbenstedt’s observed functional behavior, (2) has the added convenience of being a continuous function, and (3) has a meaningful autocorrelation function (proportional to $\exp[-\alpha|t|]$):

$$A_{v,sp}(f) = \lambda \sqrt{\frac{\pi f_{exc}^2}{12}} \sqrt{\frac{2\alpha}{\alpha^2 + (2\pi f)^2}}, \quad (12)$$

where $\alpha = 2\pi f_{exc}$ and f is the vibration frequency. Equation (12) is the amplitude noise spectrum (typically in units of micrometers per second per $\text{Hz}^{1/2}$) of the *peak* velocity. The exchange rate is equal to v_t/d , where v_t is the traverse velocity of the laser spot and d is the diameter of the laser spot. For demodulated frequencies below f_{exc} the speckle noise floor is flat and equal to $A_{v,sp}(0) = \lambda(f_{exc}/12)^{1/2}$, where $A_{v,sp}(0)$ indicates no dependence on the vibration frequency. Therefore, the speckle noise increases with increasing wavelength (because a random phase change corresponds to a larger displacement) and increasing speckle exchange rate.

The functional forms of the shot and speckle noise spectra are shown in Fig. 6. The noise floor is dominated by speckle noise at low frequencies and by shot noise at high frequencies. The knee of the speckle noise floor occurs at f_{exc} .

It should be noted that increasing the spot size only improves system performance when the speckle is dominated by translation speckle. The rate of change of boiling speckle, due to a redistribution of scatterers from surface heating or target rotation, is independent of spot size, and hence boiling speckle is not mitigated with large spots. For our application, the translational speckle exchange rate (~ 20 Hz) is much higher than the boiling speckle exchange rate ($\sim < 1$ Hz); hence, boiling speckle can be neglected.

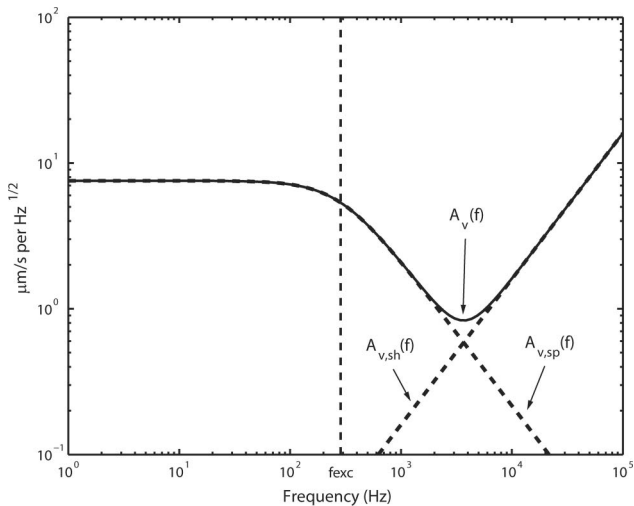


Fig. 6. Shot and speckle noise spectra. The shot noise $[A_{v,sh}(f)]$, speckle noise $[A_{v,sp}(f)]$, and total noise $[A_v(f)]$ are given by Eqs. (10), (12), and (13), respectively. The parameters used to generate these curves were $\text{CNR} = 30 \text{ dB}$, $d = 7 \text{ mm}$, and $v_t = 200 \text{ cm/s}$.

C. Vehicle Vibration

At low acoustic frequencies ($< 1000 \text{ Hz}$), the shot noise is small because of the f functional dependence [see Eq. (10)] and vehicle vibrations dominate the noise floor. This section discusses the ability to remove platform-induced clutter.

A human operator was instructed to keep the vehicle velocity constant at some value between 1–3 mph (44–134 cm/s). The vehicle speed was computed from the Doppler shift of the ladar data. It was observed that the vehicle traveled much faster than instruction, with the majority of time being around 200 cm/s (4.5 mph). The vehicle speed versus time is plotted in Fig. 7 for a 12 s interval, where the operator tried to keep a constant speed. The mean and standard deviation of the vehicle speed over the 12 s interval is 206 and 6.96 cm/s, respectively. As can be

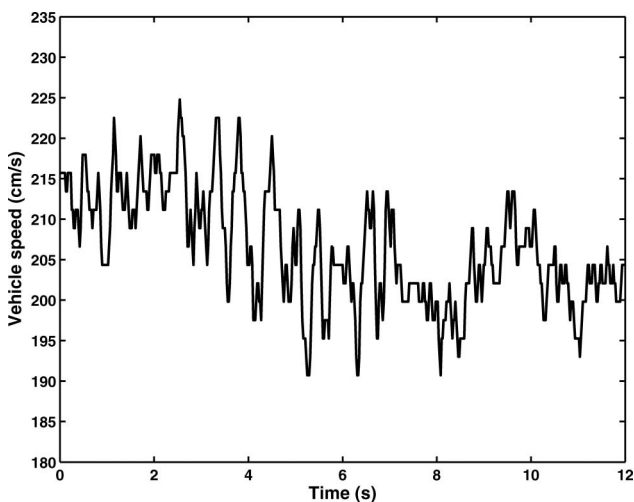


Fig. 7. Plot of vehicle speed versus time while the operator tries to maintain a constant speed.

seen, a human operator is not able to keep a very constant velocity (as robotic mounts can) and so this variation must be compensated by the Doppler tracker. The discrete NCO frequency jumps occur at the Doppler update interval, 20 ms for Fig. 7, and has a magnitude that is a multiple of 23.438 kHz (corresponding to a velocity of 1.82 cm/s).

The coherent processing interval, i.e., the interval over which the demodulated power spectra are computed, is set equal to the minimum dwell time (T_{dw}) of 1 s. The data time series was grouped into consecutive 1 s intervals and sorted into three velocity categories: 0 cm/s (parked), $100 \pm 20 \text{ cm/s}$, and $200 \pm 20 \text{ cm/s}$. The actual mean speed and standard deviation for the three categories were 0 ± 0 , 100 ± 4.5 , and $196 \pm 3.2 \text{ cm/s}$ (averaged over all 1 s intervals). We only used data from channels 1 and 3 because they had the best transmit/receive beam profile overlaps, with CNRs greater than 31 dB, and we also removed data sequences where the Doppler tracker was not locked (due to jolts).

Accelerometers (PCB Piezotronics Model 356B18; sensitivity, 1000 mV/G; frequency response, 0.5–3000 Hz) were mounted to the faces of the kinematic mounts that held the transmit collimators. The accelerometers measured the vehicle vibrations along the line of sight, and the data were used to subtract vehicle motion from all five laser vibrometer channels. The accelerometer data are shown in Fig. 8 from 30 to 46875 Hz. The power spectra at 0, 100, and 200 cm/s were averaged over 18, 26, and 34 1 s intervals, all obtained during a 640 s period. For 0 cm/s, the car motor was turned on. The three velocities 0, 100, and 200 cm/s are shown in black, dark gray, and light gray, respectively. The three smooth curves, including the straight line corresponding to 0 cm/s, are theoretical curves that will be explained later. These theoretical curves are replotted in Figs. 8–11 so that noise levels among these plots can be compared with each other. It can be seen that the

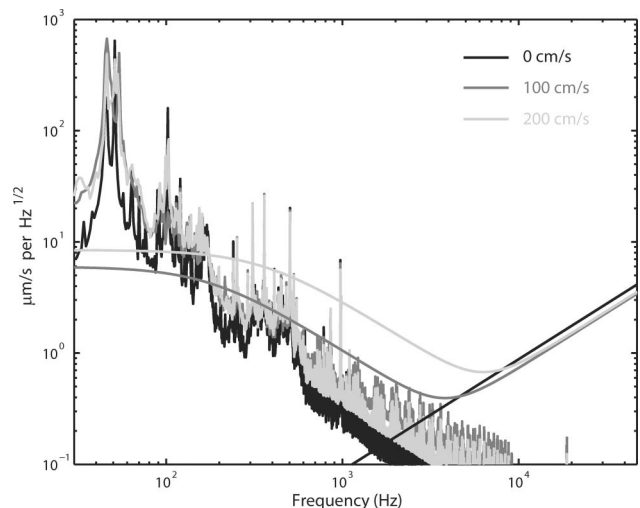


Fig. 8. Amplitude spectrum of the surface velocity as measured with a contact accelerometer. Solid smooth curves are theoretically expected noise floors due to shot and speckle noise [Eq. (13)].

platform vibrations are similar for all speeds, which indicates that the response is mainly dominated by motor vibrations above 30 Hz. No effort was taken to isolate the optical breadboard from vibrations, and we expect that the vibration coupling from the vehicle to the optical breadboard could be greatly reduced by placing vibration isolators between the optical breadboard and the vehicle roof, and by replacing the spring-loaded collimator mounts with flexure mounts.

Figures 9–11 show the amplitude spectra of the surface velocity as measured with the laser vibrometer, after various degrees of data processing. In all these figures, for each vehicle velocity, the data were averaged over all the data available for that velocity. In Fig. 9, for the 0 cm/s case, the laser vibrometer measurements at low frequencies (below ~500 Hz) are the same as the 0 cm/s accelerometer measurements (see Fig. 8). At vehicle speeds of 100 and 200 cm/s, as expected, the noise floor of the laser vibrometer in the 30–500 Hz range is higher than the accelerometer measurements, presumably due to pointing jitter. In addition, shot noise dominates at high frequencies in the laser vibrometer data, whereas it is completely absent in the accelerometer data (compare Fig. 9 with Fig. 8).

The smooth lines in Figs. 9–11 are theoretical predictions of the noise floor due to speckle and shot noise (no platform noise included) and are given by

$$A_v(f) = \sqrt{[A_{v,sh}(f)]^2 + [A_{v,sp}(f)]^2}, \quad (13)$$

where A_{sh} and A_{sp} are given by Eqs. (10) and (12), respectively. The theoretical curves in these aforementioned plots are the same in all figures and serve as a visual reference to compare the noise floors across figures. The average CNR of the data was

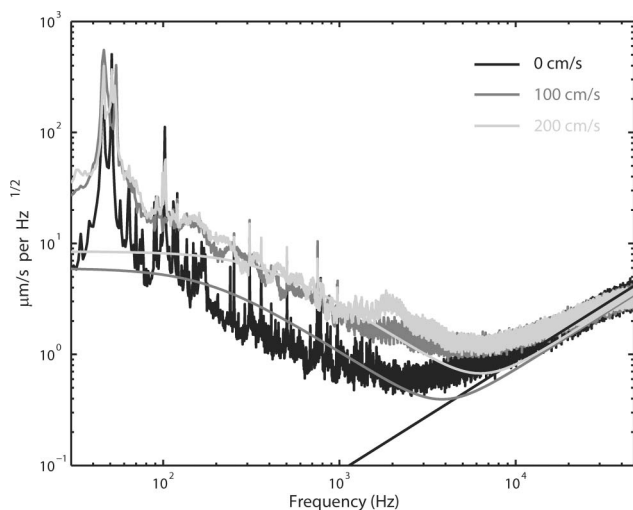


Fig. 9. Amplitude spectrum of the surface velocity as measured with the laser vibrometer, uncompensated with accelerometer data or optical reference channel. Solid smooth curves are theoretically expected noise floors due to shot and speckle noise [Eq. (13)].

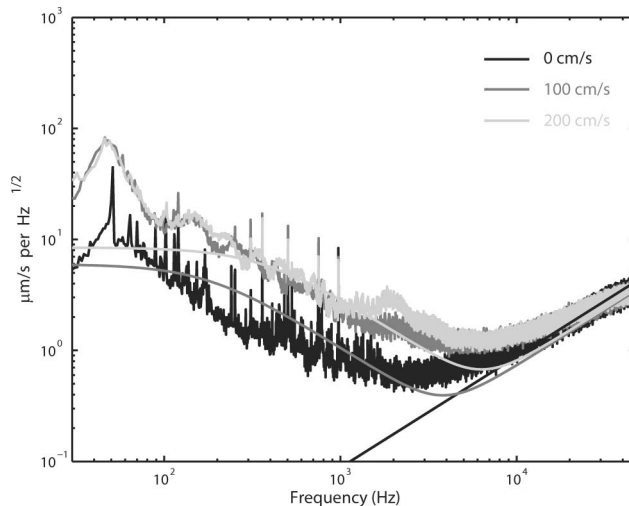


Fig. 10. Amplitude spectrum of the surface velocity as measured with the laser vibrometer, corrected with accelerometer data. Solid smooth curves are theoretically expected noise floors due to shot and speckle noise [Eq. (13)].

35.2, 36.8, and 36.5 dB for 0, 100, and 200 cm/s, respectively. The spot size was 7 mm, but during experiments, we were able to maintain an overlap between the transmit and receive spots to only within about 80%, yielding an effective spot size of 5.6 mm. The reduced effective spot diameter of 5.6 mm was used in Eq. (12).

Figure 10 shows the improved laser vibrometer noise floor after coherently subtracting the accelerometer measurements. For the 0 cm/s case, the largest noise reduction occurs at low frequencies (below 500 Hz).

Figure 11 shows the even better laser vibrometer noise floor after coherently subtracting the line-of-sight accelerometer measurements and subtracting an optical reference channel (channel 3

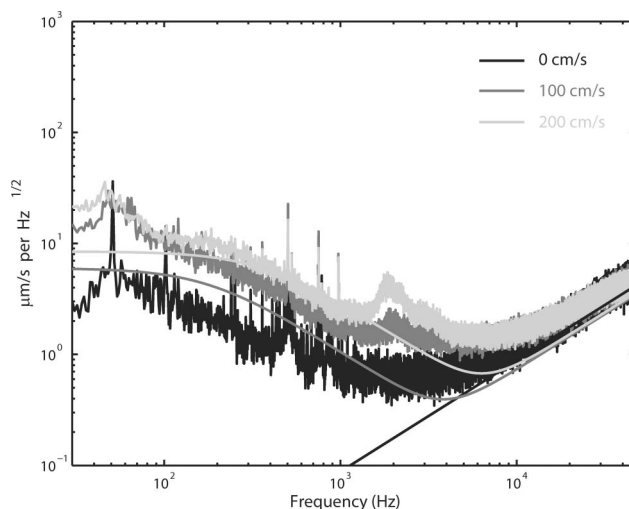


Fig. 11. Amplitude spectrum of the surface velocity as measured with the laser vibrometer, corrected with accelerometer data and optical reference channel. Solid smooth curves are theoretically expected noise floors due to shot and speckle noise [Eq. (13)].

was subtracted from channel 1). The optical reference channel must be pointed away from the target of interest, so that the sampled acoustic mode on the target surface is either out of phase or attenuated at the spatial location that is seen by the optical reference channel. Often, it is more interesting to measure the presence of a vibration rather than quantify its exact amplitude. In our tests, we simply used two channels separated by 20 cm, but the exact separation required depends on the application (low- versus high-frequency acoustic modes, how accurately the vibration amplitude must be measured, etc.). In addition, the angle between one channel and the optical reference channel causes a slight difference in the line-of-sight vibrational amplitude, an effect that must be corrected in processing to achieve the highest rejection ratio. These angular variations were not corrected in the results presented here, and hence further improvement could be expected with better processing. The most dramatic noise reduction in Fig. 11 occurs at low frequencies: compared to the uncorrected laser vibrometer noise floor (Fig. 9), the low frequency (<500 Hz) vibrations (at 0 cm/s vehicle velocity) are reduced by a factor of ~10. At high frequencies (>2 kHz), the improvement factor is actually less than 1: the noise floor after subtracting a reference channel is slightly worse at high frequencies, which is dominated by shot noise. Because the shot noise is uncorrelated between channel 1 and 3, the shot-noise energy is summed and hence the noise floor degrades by a factor of $2^{1/2}$. At a vehicle speed of 200 cm/s, our laser vibrometer approaches the speckle-and-shot-noise limit in the frequency range 300–46875 Hz.

4. Conclusions

We have demonstrated mobile laser vibrometry on a dirt road. Our laser vibrometer achieved speckle-and-shot-noise-limited performance from 300 to 46875 Hz at a speed of 200 cm/s. The success of the demonstration can be mainly attributed to the large collimated laser beam diameter of 7 mm, which reduces speckle noise. Platform vibrations, which were significant at low frequencies (<500 Hz), were compensated with accelerometers and an optical reference channel.

Our system could be improved in a number of ways. Further improvements to vehicle vibration isolation would reduce the noise floor of our system at low frequencies, e.g., by installing passive mechanical isolators for the optical breadboard, adding an accelerometer to the receive collimator (or having a single solid flexure mount for all collimators), calibrating the accelerometers more accurately, and adding gyroscopes to remove pseudovibrations due to pointing jitter. In addition, it would be desirable to switch from a bistatic to a monostatic configuration so that the size of the optical breadboard could be reduced by half; this would simplify alignment and eliminate parallax. To achieve monostatic operation on static targets, the laser waveform would need

to be pulsed to allow the system to temporally gate out facet reflections.

Even without these improvements, our laser vibrometer is the most sensitive system mounted on a moving ground vehicle reported to date.

This work is sponsored by the U.S. Air Force under AF contract FA8721-05-C-0002. Opinions, interpretations, recommendations, and conclusions are those of the authors and are not necessarily endorsed by the United States government.

References

- OYO Geospace Corporation, 7007 Pinemont Drive, Houston, Texas 77040, USA.
- PCB Piezotronics, Inc., 3425 Walden Avenue, Depew, New York 14043-2495, USA.
- Applied Technology Associates, 1300 Britt Street SE, Albuquerque, NM 87123, USA.
- R. Haupt and K. Rolt, "Acoustic detection of hidden objects and material discontinuities," U.S. patent 7,694,567 (13 April 2010).
- H. H. Nassif, M. Gindy, and J. Davis, "Comparison of laser Doppler vibrometer with contact sensors for monitoring bridge deflection and vibration," *NDT&E Int.* **38**, 213–218 (2005).
- J. R. Bell and S. J. Rothberg, "Rotational vibration measurements using laser Doppler vibrometry: comprehensive theory and practical application," *J. Sound Vib.* **238**, 673–690 (2000).
- J. Sabatier and G. Matalkah, "A study on the passive detection of clandestine tunnels," in *2008 IEEE Conference on Technologies for Homeland Security*, (IEEE, 2008), pp. 353–358.
- A. L. Kachelmyer and K. I. Schultz, "Laser vibration sensing," *Linc. Lab. J.* **8**, 3–28 (1995).
- R. Haupt and K. D. Rolt, "Stand-off acoustic-laser technique to locate buried landmines," *Linc. Lab. J.* **15**, 3–22 (2005).
- J. M. Sabatier and N. Xiang, "Laser-Doppler-based acoustic-to-seismic detection of buried mines," *Proc. SPIE* **3710**, 215–222 (1999).
- J. M. Sabatier and N. Xiang, "An investigation of acoustic-to-seismic coupling to detect buried antitank landmines," *IEEE Trans. Geosci. Remote Sens.* **39**, 1146–1154 (2001).
- N. Xiang and J. M. Sabatier, "An experimental study on antipersonnel landmine detection using acoustic-to-seismic coupling," *J. Acoust. Soc. Am.* **113**, 1333–1341 (2003).
- B. Libbey, D. Fenneman, and B. Burns, "Mobile platform for acoustic mine detection applications," *Proc. SPIE* **5794**, 683–693 (2005).
- Polytec Laser Vibrometers, 25 South Street, Suite A, Hopkinton, Massachusetts 01748, USA.
- MetroLaser, 8 Chrysler, Irvine, California 92618, USA.
- T. Writer, J. M. Sabatier, M. A. Miller, and K. D. Sherbondy, "Mine detection with a forward-moving portable laser Doppler vibrometer," *Proc. SPIE* **4742**, 649–653 (2002).
- J. M. Sabatier, "Increased ground vibration measurement speed for landmine detection," Tech. Rep. ADA514444 (University of Mississippi, 2009).
- R. D. Burgett, M. R. Bradley, M. Duncan, J. Melton, A. K. Lal, V. Aranchuk, C. F. Hess, J. M. Sabatier, and N. Xiang, "Mobile mounted laser Doppler vibrometer array for acoustic landmine detection," *Proc. SPIE* **5089**, 665–672 (2003).
- D. N. Barr, C. S. Fox, and J. E. Nettleton, "Stabilized reference surface for laser vibration sensors," U.S. patent 4,777,825 (18 October 1988).

20. H. Kim, Y. Lee, C. Kim, T.-G. Chang, and M.-S. Kang, "Laser Doppler vibrometer with body vibration compensation," *Opt. Eng.* **42**, 2291–2295 (2003).
21. C. N. Shen, B. Waeber, L. Girata, and A. R. Lovett, "Project Radiant Outlaw," *Proc. SPIE* **2272**, 63–74 (1994).
22. H. Nguyen, M. Vai, A. Heckerling, M. Eskowitz, F. Ennis, T. Anderson, L. Retherford, and G. Lambert, "Rapid—a rapid prototyping methodology for embedded systems," presented at the High Performance Embedded Computing Workshop, Lexington, Massachusetts, USA, 22–23 September 2009.
23. H. Nguyen and M. Vai, "Rapid prototyping technology," *Linc. Lab. J.* **18**, 17–27 (2010).
24. F. M. Gardner, *Phase-lock Techniques* (Wiley, 1979).
25. V. Aranchuk, A. Lal, C. Hess, and J. M. Sabatier, "Multi-beam laser Doppler vibrometer for landmine detection," *Opt. Eng.* **45**, 104302 (2006).
26. P. Gatt, S. W. Henderson, J. A. L. Thomson, and D. L. Bruns, "Micro-Doppler lidar signals and noise mechanisms: theory and experiment," *Proc. SPIE* **4035**, 422–435 (2000).
27. D. Letalick, I. Renhorn, O. Steinvall, and J. H. Shapiro, "Noise sources in laser radar systems," *Appl. Opt.* **28**, 2657–2665 (1989).
28. J. Totems, V. Jolivet, J.-P. Ovarlez, and N. Martin, "Advanced signal processing methods for pulsed laser vibrometry," *Appl. Opt.* **49**, 3967–3979 (2010).
29. K. D. Ridley and E. Jakeman, "Signal-to-noise analysis of FM demodulation in the presence of multiplicative and additive noise," *Signal Process.* **80**, 1895–1907 (2000).
30. R. L. Lucke and L. J. Rickard, "Photon-limited synthetic-aperture imaging for planet surface studies," *Appl. Opt.* **41**, 5084–5095 (2002).
31. J. W. Goodman, *Statistical Optics* (Wiley, 1985).
32. J. H. Shapiro, "Correlation scales of laser speckle in heterodyne detection," *Appl. Opt.* **24**, 1883–1888 (1985).
33. C. A. Hill, M. Harris, K. D. Ridley, E. Jakeman, and P. Lutzmann, "Lidar frequency modulation vibrometry in the presence of speckle," *Appl. Opt.* **42**, 1091–1100 (2003).
34. A. Dräbenstedt, "Quantification of displacement and velocity noise in vibrometer measurements on transversely moving or rotating surfaces," *Proc. SPIE* **6616**, 661632 (2007).